Internal photoemission for photovoltaic using *p*-type Schottky barrier: Band structure dependence and theoretical efficiency limits

Ko-Han Shih and Yin-Jung Chang[a)]
Department of Optics and Photonics, National Central University, Taoyuan, Taiwan

(Received 3 September 2017; accepted 18 December 2017; published online 12 January 2018)

Solar energy conversion via internal photoemission (IPE) across a planar *p*-type Schottky junction is quantified for aluminum (Al) and copper (Cu) in the framework of direct transitions with non-constant matrix elements. Transition probabilities and k-resolved group velocities are obtained based on pseudo-wavefunction expansions and realistic band structures using the pseudopotential method. The k-resolved number of direct transitions, hole photocurrent density, quantum yield (QY), and the power conversion efficiency (PCE) under AM1.5G solar irradiance are subsequently calculated and analyzed. For Al, the parabolic and "parallel-band" effect along the U-W-K path significantly enhances the transition rate with final energies of holes mainly within 1.41 eV below the Fermi energy. For Cu, *d*-state hot holes mostly generated near the upper edge of 3*d* bands dominate the hole photocurrent and are weekly (strongly) dependent on the barrier height (metal film thickness). Hot holes produced in the 4*s* band behave just oppositely to their *d*-state counterparts. Non-constant matrix elements are shown to be necessary for calculations of transitions due to time-harmonic perturbation in Cu. Compared with Cu, Al-based IPE in *p*-type Schottky shows the highest PCE (QY) up to about 0.2673% (5.2410%) at $\Phi_B = 0.95$ eV (0.5 eV) and a film thickness of 11 nm (20 nm). It is predicted that metals with relatively dispersionless *d* bands (such as Cu) in most cases do not outperform metals with photon-accessible parallel bands (such as Al) in photon energy conversion using a planar *p*-type Schottky junction. *Published by AIP Publishing.*
https://doi.org/10.1063/1.5003117

I. INTRODUCTION

Hot-electron-based photon energy conversion[1] in metals applied to photovoltaics[2–8] and photodetection[9–13] has gained much attention and interest in recent years. The extraction and collection of photoexcited hot electrons in metals via internal photo-emission (IPE) over a Schottky barrier have now become a common practice to deal with undesired thermalization that typically takes place within nanometer lengths and on picosecond scale. The IPE process using a metallic absorber and a Schottky barrier typically involves photon absorption that excites electrons in a metal to energy states above the Fermi energy (called "hot" electrons) followed by carrier transport and emission over or tunneling through the Schottky barrier. It is well understood that, in addition to the natural limitation imposed by the electron density of states (DOS) in metals, the existence of a dark thermionic current through the Schottky junction presents a major obstacle for bringing the conversion efficiency to any practical levels.

Although plasmon-enhanced IPE in solid-state devices has been experimentally demonstrated in various device structures[4,13–16] with the external quantum efficiency ranging from 0.01%[15] up to 8.4%[14] at the localized surface plasmon excitation frequency, theoretical efficiency limits of full-spectrum solar energy harvesting are seen only in a few literatures.[3,17–20] In most theoretical investigations, the removal of important physical principles such as conservation of electron momentum[3,17–19] or carrier dynamics and emission probability[17,19] or all of the above[17] is commonly seen due mainly to computational complexities or proper theoretical formulations. Transitions (whether direct or fully nondirect) based on realistic energy band structures, rather than a simple free-electron model, were considered perhaps only in the work of Boriskina *et al.*[19] and Chang and Shih.[20] A full, more rigorous, yet practical treatment (including realistic energy band structures, carrier dynamics, and momentum matching upon emission at the Schottky junction) in the context of direct and fully nondirect transitions with a constant matrix element is first reported in 2016.[20] It reveals that Al-based IPE through an *n*-type Schottky barrier may outperform its noble metal-based counterparts in full solar spectrum harvesting, exhibiting a maximum power conversion efficiency (PCE) of approximately 0.31% under AM1.5G solar illumination.

As has been revealed previously,[20] the energy distribution of hot electrons from *d*-bands of noble metals is of broadband character and is often closer to the Fermi energy E_F, giving rise to a strong dependence of the PCE on the barrier height. For example, a barrier height of only a few tenths of one electron volt (eV) can block a large portion of hot 3*d*-state electrons in copper (Cu). Thus the IPE from *d*-bands is shown to have little contributions to the photocurrent in an *n*-type Schottky junction, in spite of having higher DOS there due to relatively dispersionless band structure.

Despite the fact that photon energy conversion using hot (i.e., energetic) electrons from *d*-bands of noble metals may be very limited, holes photoexcited in low-lying bands often

a)Electronic mail: yjchang@ncu.edu.tw

possess higher energies with respect to E_F. This may open another window for photon energy harvesting via the IPE across p-type Schottky junctions. However, research in this aspect has been much less explored and conducted under oversimplified assumptions due perhaps to the complexities of the problem. The first work may be found in the work of Boriskina *et al.*[19] where the realistic band structure of gold (Au) and the associated DOS were considered but ballistic transport and no momentum conservation upon transition were assumed. The PCE due to hot holes is subsequently found to be >10%, as opposed to 3.6% from hot electrons, under standard AM1.5D solar illumination. As the theoretical efficiency estimates can be tremendously different with different underlying assumptions, the results thus reported may overestimate the performance of a p-type Schottky device in photon energy conversion.

In this paper, solar energy conversion via the IPE across a p-type planar Schottky junction is theoretically and rigorously investigated in the framework of direct transitions with non-constant matrix elements. Position-dependent photon absorption, realistic energy band structure, carrier transport, and momentum matching upon emission across the junction interface are all fully treated. In particular, **k**-resolved group velocities are obtained to quantify inelastic scattering as a function of carrier energy, making carrier transport also band structure dependent. Pseudopotential formulation of the matrix element for transitions due to time-harmonic perturbation and band structure dependence of the hole photocurrent density in Cu (as a representative case) are reported for the first time. With the absorption depth considered, how the band structure, barrier height (energy), and the metal film thickness together affect the hole photocurrent density, quantum yield (QY), and the PCE in such a system are revealed and deliberated. As far as photovoltaic is concerned, we show that metals with relatively dispersionless d bands (such as Cu) in most cases do not outperform metals with photon-accessible parallel bands (such as Al) in planar p-type Schottky junctions.

II. THEORETICAL FORMALISM

Consider a p-type Schottky junction formed by a planar metal film of thickness t and p-type semiconductor [Fig. 1(a)] is illuminated by AM1.5G solar irradiance at the air-metal interface. In Fig. 1(b) and throughout this work, we have assumed $\Phi_m \leq \Phi_s$, where Φ_m and Φ_s denote the work functions of metal and p-type semiconductor materials, respectively. Since the light reflectance $R(\nu)$ merely presents a constant multiplier at each frequency ν for the calculations hereafter, it is ignored within the entire solar spectrum for simplicity. On the other hand, the spatial dependence of the optical intensity $I(\nu, z)$ within the metal is given by Beer's law,[21] $I(z,\nu) = I_\nu e^{-\alpha(\nu)(t-z)} d\nu$, where I_ν represents the solar spectral irradiance (in units of μW/nm/cm^2) at $z = t$, and $\alpha(\nu)$ the absorption coefficient of the metal.[22] As shown in Fig. 1(b), since electrons and holes are generated in pairs, the initial (final) energy level E_i (E_f) of an electron may be treated as the final (initial) energy $E_{f,h}$ ($E_{i,h}$) of a hole and vice versa.

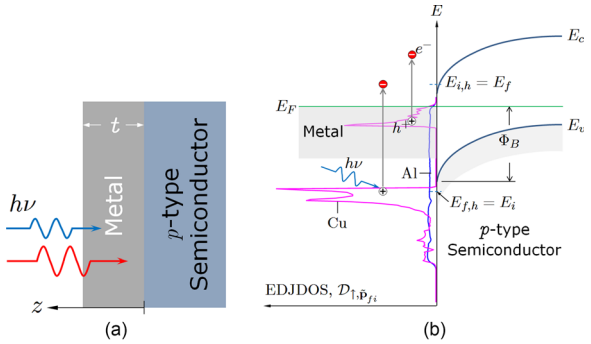

FIG. 1. (a) Schematic drawing of a p-type Schottky junction and (b) excitation of electrons in a metal from below the Fermi energy E_F to unoccupied states above E_F, creating hot holes. The Schottky barrier height is denoted by Φ_B. The energy distribution of joint density of states (EDJDOS) with non-constant optical matrix elements $\mathcal{D}_{\uparrow,\tilde{\mathbf{p}}_{fi}}$ for Al and Cu at some photon energy has been superimposed upon the energy band diagram.

We further define the excess energy of a photoexcited hole as its energy with respect to E_F: $E_{ex} = E_{f,h} - E_F$.

A. EDJDOS with non-constant matrix elements

In semiconductors, the assumption of constant momentum matrix elements leads to the well-known optical joint density of states (JDOS). This has been applied to the definition of the energy distribution of joint density of states (EDJDOS) first stated in the work of Koyama and Smith[23] and further improved in our previous work.[20] However, as opposed to semiconductors, this assumption may not be appropriate for electron transitions in a metal since they typically occur over a wider spread of wavevector **k** in the first Brillouin zone (FBZ) due to either very small or zero band gap. The dependence of transition probabilities on **k** may be more pronounced with the increase in discrepancies of wavefunctions between initial i and final f energy states. To accurately determine the energy distribution of photoexcited carriers in a metal, the transition probability described by the momentum matrix element in each allowed transition pair must be addressed.

The position-dependent total upward transition rate per unit volume, expressed from the electron point of view and taking into account the occupancy probabilities, is given by[24]

$$R_\uparrow(h\nu, \mathbf{r}) = \frac{2}{\Omega}\sum_{\mathbf{k}_f}\sum_{\mathbf{k}_i}\frac{2\pi}{\hbar}|H'_{fi}(\nu,\mathbf{r})|^2 f(E_{i,\mathbf{k}_i}) \times \left[1 - f(E_{f,\mathbf{k}_f})\right]\delta\left(E_{f,\mathbf{k}_f} - E_{i,\mathbf{k}_i} - h\nu\right), \quad (1)$$

where $\hbar$ is the reduced Planck constant, **r** denotes the position vector, Ω the volume of the crystal, $f(E)$ the Fermi-Dirac probability function, δ the Kronecker delta function, and $H'_{fi}(\nu,\mathbf{r})$ the optical matrix element. In the presence of time-harmonic perturbation, $H'_{fi}(\nu,\mathbf{r})$ can be further written as

$$H'_{fi}(\nu,\mathbf{r}) = \frac{eE_0(\nu,\mathbf{r})}{2m_0\omega}\delta_{\mathbf{k}_f,\mathbf{k}_i}\hat{\mathbf{a}}_E \cdot \tilde{\mathbf{p}}_{fi}, \quad (2)$$

with

$$\tilde{\mathbf{p}}_{fi} \equiv \langle \psi_{f,\mathbf{k}_f} | \tilde{\mathbf{p}} | \psi_{i,\mathbf{k}_i} \rangle, \tag{3}$$

where e is the elementary charge, $E_0(\nu, \mathbf{r})$ represents the amplitude of a time-harmonic electric field at frequency ν, m_0 the rest mass of an electron, ω the angular frequency, $\hat{\mathbf{a}}_E$ the unit vector of the polarization direction, $\tilde{\mathbf{p}}$ the linear momentum operator, and $\tilde{\mathbf{p}}_{fi}$ the momentum matrix element.

Equation (1) plays a central role in understanding the energy distribution of all photoexcited carriers quantified by the EDJDOS. Similar to the one with a constant $H'_{fi}(\nu, \mathbf{r})$,[20] the EDJDOS in the presence of non-constant $H'_{fi}(\nu, \mathbf{r})$ under direct transition approximation (i.e., $\mathbf{k}_i \approx \mathbf{k}_f \equiv \mathbf{k}$) is written as

$$\begin{aligned}\mathcal{D}_{\uparrow,\tilde{\mathbf{p}}_{fi}}(E_f, \nu, \mathbf{r}) = {} & \frac{e^2 E_0^2(\nu, \mathbf{r})}{16\pi^3 m_0^2 h\nu^2} \sum_{i,f} \int_{\mathrm{FBZ}} |\hat{\mathbf{a}}_E \cdot \tilde{\mathbf{p}}_{fi}|^2 f(E_{i,\mathbf{k}}) \\ & \times \left[1 - f(E_{f,\mathbf{k}})\right] \delta[E_{f,\mathbf{k}} - E_{i,\mathbf{k}} - h\nu] \\ & \times \delta(E - E_{i,\mathbf{k}}) d^3\mathbf{k}. \end{aligned} \tag{4}$$

The first Kronecker delta function ensures energy conservation with $E_{f,\mathbf{k}} = E_{i,\mathbf{k}} + h\nu$ (i.e., $E_{i,h,\mathbf{k}} = E_{f,h,\mathbf{k}} + h\nu$), while the second one selects all electron (hole) transitions having initial (final) states lying at $E_{i,\mathbf{k}}$ ($E_{f,h,\mathbf{k}}$). The delta function may be further approximated by a normalized Lorentzian function with a full-width-at-half-maximum of $\hbar/(2\tau)$ to reflect the broadening effect of each state. In this work, 11.5 fs and 35.6 fs are used for Al and Cu,[25] respectively. Physically, the quantity $\mathcal{D}_{\uparrow,\tilde{\mathbf{p}}_{fi}} dE_{f,h}$ represents the total number of holes generated per second lying between $E_{f,h}$ and $E_{f,h} + dE_{f,h}$ due to photons at $h\nu$ per unit volume at position $\mathbf{r}$.

B. Pseudopotential formulation of momentum matrix element

Following our previous work[20] where the pseudopotential method[26–29] was applied to calculate realistic band structures of Al, Cu, and silver (Ag), the pseudopotential formulation of momentum matrix element $\tilde{\mathbf{p}}_{fi}$ is pursued in this work. In the pseudopotential method, a normalized pseudo-wavefunction $|\varphi_{u,\mathbf{k}}\rangle$ of state u is described by normalized plane waves $|\mathbf{k} + \mathbf{G}\rangle$[27]

$$|\varphi_{u,\mathbf{k}}\rangle = \frac{1}{\sqrt{\Omega}} \sum_{\mathbf{G}} C_{u,\mathbf{G},\mathbf{k}} |\mathbf{k} + \mathbf{G}\rangle, \tag{5}$$

where $\mathbf{G}$ denotes the reciprocal lattice vector and $|\varphi_{u,\mathbf{k}}\rangle$ satisfies the normalization condition $\langle \varphi_{u,\mathbf{k}} | \varphi_{u,\mathbf{k}} \rangle = 1$. The actual wavefunction of conduction-band states is related to the pseudo-wavefunction by[27]

$$|\psi_{u,\mathbf{k}}\rangle = \frac{1}{N_{u,\mathbf{k}}} \left(1 - \tilde{P}_{pro}\right) |\varphi_{u,\mathbf{k}}\rangle, \tag{6}$$

where $N_{u,\mathbf{k}}$ is the normalization constant and $\tilde{P}_{pro} = \sum_b |\psi_b\rangle\langle\psi_b|$ denotes the projection operator that projects any function onto the core states $|\psi_b\rangle$ with $b = (n, l, m)$ being the corresponding set of quantum numbers. Substituting Eqs. (5) and (6) into Eq. (3) yields

$$\begin{aligned}\langle \psi_{f,\mathbf{k}} | \tilde{\mathbf{p}} | \psi_{i,\mathbf{k}} \rangle = {} & \frac{1}{N_{f,\mathbf{k}} N_{i,\mathbf{k}}} \left(\langle \varphi_{f,\mathbf{k}} | \tilde{\mathbf{p}} | \varphi_{i,\mathbf{k}} \rangle \right. \\ & - \langle \varphi_{f,\mathbf{k}} | \tilde{\mathbf{p}} \tilde{P}_{pro} | \varphi_{i,\mathbf{k}} \rangle - \langle \varphi_{f,\mathbf{k}} | \tilde{P}_{pro} \tilde{\mathbf{p}} | \varphi_{i,\mathbf{k}} \rangle \\ & \left. + \langle \varphi_{f,\mathbf{k}} | \tilde{P}_{pro} \tilde{\mathbf{p}} \tilde{P}_{pro} | \varphi_{i,\mathbf{k}} \rangle \right), \end{aligned} \tag{7}$$

where

$$N_{u,\mathbf{k}} = \left(1 - \sum_{n,l} \sum_{\mathbf{G},\mathbf{G}'} C^*_{u,\mathbf{G},\mathbf{k}} C_{u,\mathbf{G}',\mathbf{k}} \underline{\underline{\mathbf{S}}}_{l,\mathbf{K},\mathbf{K}'} A_{n,l,\mathbf{K}} A_{n,l,\mathbf{K}'} \right)^{1/2}; \quad u = \{i, f\}, \tag{8}$$

$$\langle \varphi_{f,\mathbf{k}} | \tilde{\mathbf{p}} | \varphi_{i,\mathbf{k}} \rangle = \sum_{\mathbf{G}} C^*_{f,\mathbf{G},\mathbf{k}} C_{i,\mathbf{G},\mathbf{k}} \hbar(\mathbf{k} + \mathbf{G}), \tag{9}$$

$$\begin{aligned} & \langle \varphi_{f,\mathbf{k}} | \tilde{\mathbf{p}} \tilde{P}_{pro} | \varphi_{i,\mathbf{k}} \rangle + \langle \varphi_{f,\mathbf{k}} | \tilde{P}_{pro} \tilde{\mathbf{p}} | \varphi_{i,\mathbf{k}} \rangle \\ & = \sum_{n,l} \sum_{\mathbf{G},\mathbf{G}'} C^*_{f,\mathbf{G}',\mathbf{k}} C_{i,\mathbf{G},\mathbf{k}} \hbar(\mathbf{K} + \mathbf{K}') S_{l,\mathbf{K},\mathbf{K}'} A_{n,l,\mathbf{K}'} A_{n,l,\mathbf{K}}, \end{aligned} \tag{10}$$

$$\begin{aligned}\langle \varphi_{f,\mathbf{k}} | \tilde{P}_{pro} \tilde{\mathbf{p}} \tilde{P}_{pro} | \varphi_{i,\mathbf{k}} \rangle = {} & \sum_{n',l',m'} \sum_{\mathbf{G}'} C^*_{f,\mathbf{G}',\mathbf{k}} D^*_{\mathbf{K}',n',l',m'} \\ & \times \sum_{n,l,m} \sum_{\mathbf{G}} C_{i,\mathbf{G},\mathbf{k}} D_{\mathbf{K},n,l,m} \\ & \times \left[\sum_{j''} e^{-i\mathbf{k}\cdot\mathbf{R}_{j''}} \int_{\Omega} \phi^*_{b'}(\mathbf{r}' - \mathbf{R}_{j''}) \right. \\ & \left. \times \frac{\hbar}{i} \nabla \phi_b(\mathbf{r}') d^3\mathbf{r}' \right], \end{aligned} \tag{11}$$

with

$$A_{n,l,\mathbf{K}} \equiv \int_0^\infty j_l(Kr) R_{n,l}(r) r^2 dr, \tag{12}$$

$$S_{l,\mathbf{K},\mathbf{K}'} \equiv \frac{4\pi(2l+1)}{\Omega_c} P_l(\hat{\mathbf{a}}_K \cdot \hat{\mathbf{a}}_{K'}), \tag{13}$$

and

$$D_{\mathbf{K},n,l,m} \equiv \frac{4\pi}{\sqrt{\Omega_c}} Y^*_{l,m}(\theta_{\hat{\mathbf{a}}_K}, \phi_{\hat{\mathbf{a}}_K}) (i)^l A_{n,l,\mathbf{K}}. \tag{14}$$

In preceding equations, $\mathbf{K} \equiv \mathbf{k} + \mathbf{G}$, $\mathbf{K}' \equiv \mathbf{k} + \mathbf{G}'$, $j_l(Kr)$ is the spherical Bessel function of the first kind of order l, $R_{n,l}(r)$ the radial part of the core-state wavefunction $\phi_{n,l,m}(r, \theta, \phi)$, Ω_c the volume of a primitive cell, $P_l(\hat{\mathbf{a}}_K \cdot \hat{\mathbf{a}}_{K'})$ the Legendre polynomial, and $\hat{\mathbf{a}}_K$ and $\hat{\mathbf{a}}_{K'}$ denote the unit vectors of $\mathbf{K}$ and $\mathbf{K}'$, respectively. In this work, the core-state wavefunctions $|\psi_b\rangle$ of Al and Cu are approximated by $2s$ and $2p$ and $3s$ and $3p$ hydrogenic orbitals with effective atomic numbers Z_{eff} 9.0 and 13.5, respectively.[29,30] Moreover, in Eq. (11), the integral involving two atomic orbitals shifted by $\mathbf{R}_{j''}$ is carried out numerically and only the two nearest atoms relative to the reference atom are considered.

Figure 2 shows the non-constant-$\tilde{\mathbf{p}}_{fi}$-based EDJDOS [Eq. (4)] calculations for two representative metals, Al and Cu. Since $E_0 = 1$ V/m is assumed within the solar spectral range, the corresponding photon flux per unit light intensity decreases with frequency. For Al [Fig. 2(a)], the EDJDOS with $\tilde{\mathbf{p}}_{fi}$ (or simply, the EDJDOS hereafter) surging at

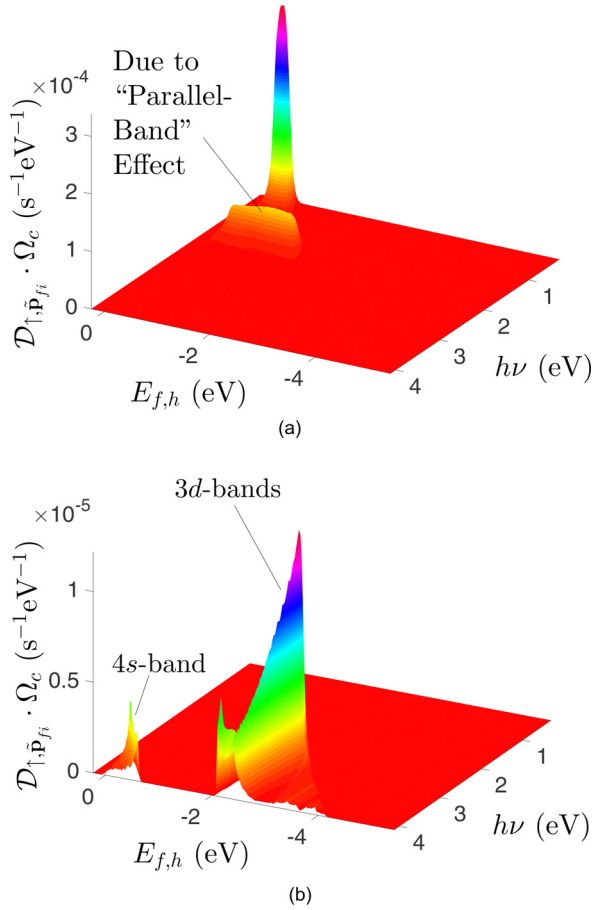

FIG. 2. Calculated EDJDOS with non-constant matrix elements H'_{fi}'s [Eq. (4)] of (a) Al and (b) Cu in the context of direct transitions. The Fermi energy E_F is used as the energy reference (0 eV). The incident electric field $E_0 = 1$ V/m [Eq. (2)] is assumed and a total of 1 366 101 **k** points are considered. Note that the z axis is $\mathcal{D}_{\uparrow,\tilde{\mathbf{p}}_{fi}} \cdot \Omega_c$ (in units of $\mathrm{s}^{-1}\mathrm{eV}^{-1}$).

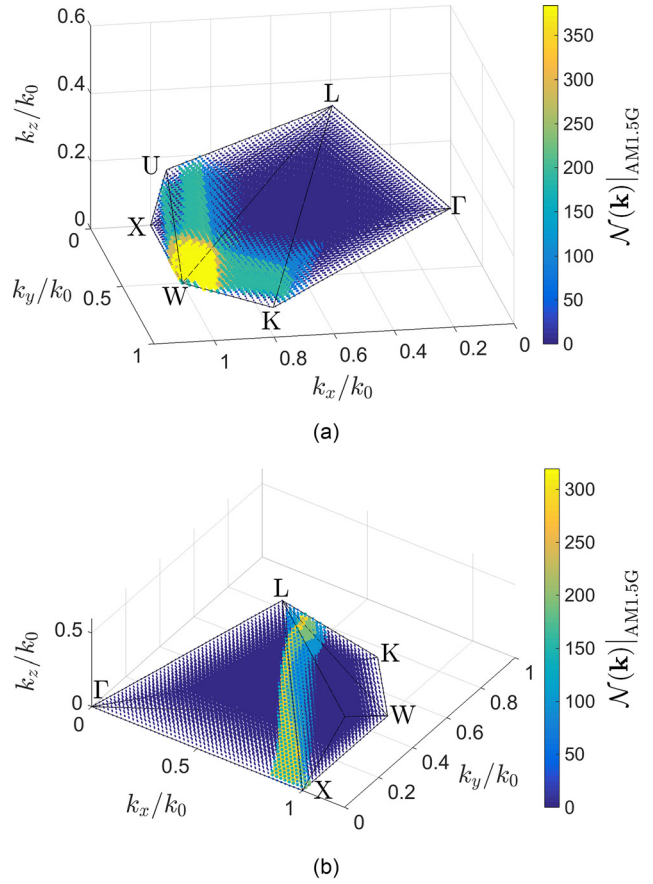

FIG. 3. Distribution of the number of allowed direct transitions $\mathcal{N}(\mathbf{k})$ due to AM1.5G solar irradiance as a function of **k** in (a) Al and (b) Cu. A total of 22 932 **k** points is used for visualization purpose. In obtaining the **k**-resolved plots, $H'_{fi} = 1$ is used for simplicity. In (b), the corridor-like, nonzero $\mathcal{N}(\mathbf{k})$ is part of the vertical slab-like $\mathcal{N}(\mathbf{k})$ distribution passing the neighborhood of the L and X points.

shallow $E_{f,h}$'s and a small range of $h\nu$ corresponds to transitions in the neighborhood of the W point in the energy band structures. A smaller but quite uniform distribution of the EDJDOS in the interval $E_{f,h} \approx [-0.03, -1.41]$ eV and $h\nu \approx [1.24, 1.63]$ eV is mainly due to the "parallel band" along the U-W-K path, in particular, near the W and K points. This is readily seen in Fig. 3(a) where the **k**-resolved number of direct transitions due to AM1.5G solar irradiance in the (1/48)-th irreducible part of the FBZ is shown.

For Cu, the number of electron transitions (hole generations) from (in) the 4s band [Fig. 2(b)] is shown to be comparable to that from (in) the 3d bands in the presence of non-constant matrix elements H'_{fi}'s. The allowed transitions from 4s states occur mainly in the **k** region close to the L point [Fig. 3(b)]. These transitions are of narrowband character in both the hole final energy and photon energy spectra ($E_{f,h} \approx [0.08, -0.67]$ eV, $h\nu \approx [3.49, 4.12]$ eV). On the other hand, transitions from 3d to 4s states are found to occur mostly near the upper edge of the 3d bands ($E_{f,h} \approx [-2.08, -2.44]$ eV) by a relatively broad range of $h\nu \approx [2.23, 4.12]$ eV. They correspond to the vertical slab-like region passing the vicinity of the L and X points in Fig. 3(b). As $E_{f,h}$ in 3d bands deviates further away from E_F, the hole generation rate is seen slightly increasing with $h\nu$ but is still very limited.

C. k-resolved group velocity and mean free path for hole transport

The research in this aspect is the cornerstone of obtaining hole transport characteristics described in terms of the hole mean free path (MFP). The results are of paramount importance in quantifying the IPE process with non-ballistic transport. Depending on the dispersion of an energy band, the group velocity $\boldsymbol{v}_{g,\mathbf{k}}$ associated with a carrier of energy $E_{\mathbf{k}}$ is **k**-dependent and is expressed as[31]

$$\boldsymbol{v}_{g,\mathbf{k}} = (1/\hbar)\nabla_{\mathbf{k}} E_{\mathbf{k}}, \tag{15}$$

where $\nabla_{\mathbf{k}}$ denotes the gradient in **k** space. To obtain the average magnitude of the group velocity as a function of energy level $\langle|\boldsymbol{v}_{g,\mathbf{k}}(E)|\rangle$, a large number of cubic grids of volume δk^3 in **k** space were created and the corresponding eigenvalues $E_{\mathbf{k}}$'s were computed. Computationally, the derivative of $E_{\mathbf{k}}$ in each direction of $\nabla_{\mathbf{k}}$ can be approximated by the central difference equation. The average group velocity (magnitude) $\langle|\boldsymbol{v}_{g,\mathbf{k}}(E)|\rangle$ within a differential energy interval centered at E was obtained accordingly.

Figure 4(a) depicts the energy-dependent $\langle|\boldsymbol{v}_{g,\mathbf{k}}(E)|\rangle$ for Al, Cu, and Ag, along with that of free electrons for comparisons. As observed, $\langle|\boldsymbol{v}_{g,\mathbf{k}}(E)|\rangle$ in Al matches very well with that of free electrons for $E < E_F - 4.829$ eV. The difference

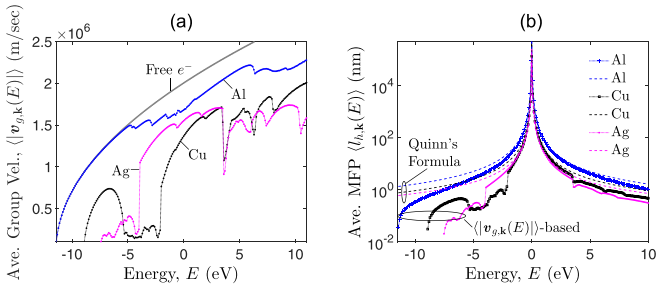

FIG. 4. The average group velocity (magnitude) $\langle|\boldsymbol{v}_{g,\mathbf{k}}(E)|\rangle$ (a) and the associated average mean free path of holes $\langle l_{h,\mathbf{k}}(E)\rangle$ (b) as a function of energy level E, where the Fermi energy is at 0 eV. The number of sampling $\mathbf{k}$ points is 174 926 and the energy interval is 0.1 eV.

between the two becomes significant with the increasing energy level because of significant departures from the free-electron model at the Brillouin zone boundaries and the increasing complexity of the band structure. For Cu and Ag, a precipitous drop in $\langle|\boldsymbol{v}_{g,\mathbf{k}}(E)|\rangle$ is clearly seen at their corresponding interband absorption edge (Cu: $\approx$2 eV and Ag: $\approx$4 eV below E_F) as a result of the relatively dispersionless band structure there; the $\langle|\boldsymbol{v}_{g,\mathbf{k}}(E)|\rangle$ remains low over the entire energy interval of d bands.

The MFP of holes averaged over $\mathbf{k}$ points at energy level E $\langle l_{h,\mathbf{k}}(E)\rangle$ used to describe the relaxation process during carrier transport may be written as $\langle l_{h,\mathbf{k}}(E)\rangle = \langle|\boldsymbol{v}_{g,\mathbf{k}}(E)|\rangle\tau_h(E)$,[25] where $\tau_h(E)$ denotes the carrier lifetime of holes at energy E. For simplicity, the Auger effect on lifetime estimates for d-band holes is ignored and $\tau_h(E)$ may be estimated based on the free-carrier model[32]

$$\tau_h(E) = \tau_0 \frac{E_F^2}{(E - E_F)^2}, \tag{16}$$

where τ_0 is a material-dependent prefactor and is 0.35, 0.50, and 0.60 for Al, Cu, and Ag, respectively.[32] The average MFP of holes thus obtained with varying energies is given in Fig. 4(b). Also shown in the figure are the results (dashed lines) from Quinn's analytical formula for the MFP due to inelastic electron-electron (e-e) scattering in metals[33]

$$l_{e-e} = 4(1 + r_s)\frac{(E_{ex} + E_F)E_F}{E_{ex}^2}, \tag{17}$$

where r_s denotes the radius parameter of a metal and is 2.07, 2.67, and 3.02 for Al, Cu, and Ag,[34] respectively. In general, results from Quinn's formula are in good agreement with the numerical, $\langle|\boldsymbol{v}_{g,\mathbf{k}}(E)|\rangle$-based computations near and above E_F. The difference between the two becomes increasingly large as the energy deviates from E_F, particularly for Cu and Ag and for energies below E_F (0 eV). Moreover, the asymmetric dependence of the MFP on the energy is clearly seen due solely to the asymmetry of the band structure with respect to E_F. For example, hot holes in Cu (Ag) at $E_{f,h} \approx -2.22$ eV (-4.22 eV) have a MFP of only around 1.01 nm (0.20 nm), as opposed to approximately 7.60 nm (1.43 nm) for hot electrons with $E_f \approx 2.28$ eV (4.28 eV). Hot holes in d bands are therefore shown to have a much shorter MFP than that of hot electrons at the energy level symmetric to E_F.

D. Derivation of the IPE-based photocurrent density J_{ph}

Following the EDJDOS formalism with non-constant H'_{fi} and the treatment of the MFP based on realistic band structures, the photocurrent from the IPE-based solar energy conversion is addressed in this sub-section. It should be emphasized that the formalism presented here is not restricted to the hot holes emitted across a planar p-type Schottky junction, but is applicable to the IPE of all carrier species across a metal-semiconductor or metal-dielectric interface. In addition, we intended to express the photocurrent in terms of the time-harmonic electric field $\mathbf{E}(\nu, \mathbf{r})$ ($\mathbf{r}$: the position vector) within the metal so that the final expression may also apply to more complicated metallic nanostructures once the spatial distribution of $\mathbf{E}(\nu, \mathbf{r})$ is known.

The generation rate of photoexcited carriers per unit volume with energies falling between E'_f and $E'_f + dE'_f$ (in $s^{-1}cm^{-3}$) due to photons of $h\nu$, may be expressed as $\mathcal{D}_{\uparrow,\tilde{\mathbf{p}}_{fi}}(E'_f, \nu, \mathbf{r})dE'_f$. The general expression for the spectral photocurrent $I_{ph,\nu}(\nu)$ in a metal of volume Ω is then written as

$$I_{ph,\nu}(\nu) = e\int_{\Delta E'_f(\nu)}\int_{\Omega} P_{r-e}(\mathbf{r}, E'_f)\mathcal{D}_{\uparrow,\tilde{\mathbf{p}}_{fi}}(E'_f, \nu, \mathbf{r})d^3\mathbf{r}dE'_f, \tag{18}$$

where $P_{r-e}(\mathbf{r}, E'_f)$ is the probability for a hot carrier of energy E'_f to reach and emit across the Schottky junction. For a one-dimensional (1-D) problem with a metal film of thickness t, neglecting the tunneling effect and the reflection due to potential difference[1] and assuming specular reflection and elastic scattering at the air-metal interface, we obtain

$$P_{r-e}(z, E'_f) = \frac{1}{2}\int_0^{\theta_{\max}} \exp\left[\frac{-z}{\langle l_{h,\mathbf{k}}(E'_f)\rangle\cos\theta}\right] \times \left\{1+\exp\left[\frac{-2(t-z)}{\langle l_{h,\mathbf{k}}(E'_f)\rangle\cos\theta}\right]\right\}\sin\theta d\theta \tag{19}$$

with $\theta_{\max} = \cos^{-1}(\Phi_B/|E'_f - E_F|)^{1/2}$ being the largest half-opening angle of the permitted emission cone. Since the field amplitude $E_0(\nu, \mathbf{r})$ in $\mathcal{D}_{\uparrow,\tilde{\mathbf{p}}_{fi}}(E'_f, \nu, \mathbf{r})$ [Eq. (4)] is z-dependent in the present 1-D case, we apply the Beer's law and the time-average Poynting vector of a plane wave in a lossy material to obtain

$$E_0^2(\nu, z) = 2I_\nu\left\{\mathrm{Re}\left[\frac{1}{\eta_c^*(\nu)}\right]\right\}^{-1} e^{-\alpha(t-z)}d\nu, \tag{20}$$

where $\eta_c(\nu)$ denotes the complex impedance of the metal and the asterisk represents the complex conjugate. Combining Eqs. (4), (18), and (20) yields the total photocurrent density J_{ph}

$$J_{ph} = \frac{2e}{h\nu}\cdot\frac{e^2}{16\pi^3 m_0^2\nu}\int_{\mathrm{Solar}}\int_{\Delta E'_f(\nu)}\int_0^t P_{r-e}(z, E'_f)I_\nu \times\left\{\mathrm{Re}\left[\frac{1}{\eta_c^*(\nu)}\right]\right\}^{-1} e^{-\alpha(t-z)} \times\left\{\sum_{i,f}\int_{\mathrm{FBZ}}|\hat{\mathbf{a}}_E\cdot\tilde{\mathbf{p}}_{fi}|^2\times f(E'_{i,\mathbf{k}})\left[1-f(E'_{f,\mathbf{k}})\right]\delta \times\left[E'_{f,\mathbf{k}} - E'_{i,\mathbf{k}} - h\nu\right]\times\delta\left(E - E'_{i,\mathbf{k}}\right)d^3\mathbf{k}\right\}dzdE'_f d\nu. \tag{21}$$

Note that the E'_f range over which the integrals in Eqs. (18) and (21) are carried out is also frequency dependent, as clearly seen in Fig. 2.

III. RESULTS AND DISCUSSIONS

A. Band structure dependence of IPE-based hole photocurrent density $J_{ph}^{(h)}$

In investigations of the band structure dependence of the IPE of holes, we take Cu as the representative case since the hole generation rate in the 4*d*-bands of Ag is expected to be significantly smaller within the solar spectrum owing to Ag's deep interband absorption edge. Also, as the overlap of 3*d* bands and the 4*s* band in Cu makes it difficult to accurately distinguish their individual contributions to the hole photocurrent density $J_{ph}^{(h)}$, the $E_{f,h}$ boundary separating the two is set to $E_{f,h} = -2.10$ eV (i.e., 2.10 eV below E_F).

Figure 5 shows the $J_{ph,d-\text{band}}^{(h)}$ and $J_{ph,s-\text{band}}^{(h)}$ from a 20-nm-thick Cu-*p*-type Schottky barrier in the framework of direct transitions. Due to the interband absorption threshold in Cu (about 2.10 eV below E_F),[22] $J_{ph,d-\text{band}}^{(h)}$ becomes appreciable only if $h\nu > 2.25$ eV for all Φ_B's of interest [Fig. 5(a)]. Also, the photon energy at which the peak $J_{ph,d-\text{band}}^{(h)}$ occurs remains at 2.50 eV, despite the change in Φ_B. This may be understood by referring to Fig. 5(d) where the EDJDOS of Cu peaks at $h\nu \approx 2.44$ eV and remains high for $h\nu \approx [2.32, 2.86]$ eV and $E_f \approx [-2.29, -2.41]$ eV. In addition to the high EDJDOS distribution, hot holes produced within this $E_{f,h}$ range (i.e., near the upper edge of 3*d* bands) typically possess relatively smaller excess energies when compared to those at $E_{f,h}$'s further down away from E_F. It then becomes natural to see a larger $J_{ph,d-\text{band}}^{(h)}$ in this range of $h\nu$ in Fig. 5(a).

On the other hand, the EDJDOS $\mathcal{D}_{\uparrow,\tilde{\mathbf{p}}_{fi}}$ and Φ_B together shape the frequency dependence of $J_{ph,d-\text{band}}^{(h)}$, in addition to the influence of solar irradiance spectrum. As shown in Fig. 5(d), photons with higher energies may populate hot holes to a broader range of final energies, causing the broadening of the EDJDOS in $E_{f,h}$ spectrum. As $E_{f,h}$ moves away from E_F, the MFP (averaged over all **k** points at the same energy level) drops precipitously [Fig. 4(b)] but the permitted emission cone gets larger ($E_{ex}\cos\theta > \Phi_B$ at the material interface). These two effects offset each other at lower $E_{f,h}$'s, while the MFP becomes dominant at higher $E_{f,h}$'s, giving rise to a fast decreasing $J_{ph,d-\text{band}}^{(h)}$ with $h\nu$. The frequency bandwidth of $J_{ph,d-\text{band}}^{(h)}$ is also shown to be independent of Φ_B of interest in Fig. 5(a) since hot holes produced in 3*d* bands have sufficient kinetic energies to overcome the barrier.

As opposed to $J_{ph,d-\text{band}}^{(h)}$, the hole photocurrent density from the *s* band $J_{ph,s-\text{band}}^{(h)}$ is of narrowband character in Cu, exhibiting a high photon energy threshold and a strong dependence on Φ_B [Fig. 5(b)]. Referring to Figs. 5(c) and 5(d), these characteristics are a direct consequence of large energy differences between bands 6 (4*s*) and 7 around the L point and between bands 5 and 6 around the X point. For $\Phi_B = [0.1, 0.2]$ eV, the onset $h\nu$ for a nonzero $J_{ph,s-\text{band}}^{(h)}$ corresponds to the energy required to generate hot holes just below E_F in the neighborhood of the L point. Contributions from band 5 around the X point are revealed only when Φ_B is sufficiently large to fully block those from around the L point, leading to a fixed photon energy threshold at 3.78 eV.

The nonzero $J_{ph,s-\text{band}}^{(h)}$'s for $\Phi_B > 0.5$ eV in Fig. 5(b), which may seem unreasonable at first glance, is actually contributed by the very top edge of 3*d* bands with $E_{f,h} > -2.10$ eV. As indicated in Fig. 5(d), since $J_{ph,s-\text{band}}^{(h)}$ is calculated from all hot holes with $E'_f\text{s} > -2.10$ eV, the EDJDOS broadening (with an increasing $h\nu$) associated with 3*d* bands results in nonzero but very small amount of hole generations in the energy interval $E_f \approx [-2.07, -2.10)$ eV. Further investigations show that for $\Phi_B < 0.7$ eV, hot holes generated in the 4*s* band around the L point overwhelmingly dominate $J_{ph,s-\text{band}}^{(h)}$.

B. Dependence of photocurrent density on the metal thickness

Generally speaking, since the barrier height is measured in opposite directions from E_F for *n*- and *p*-type Schottky junctions, the hole photocurrent density from the *p*-type Schottky behaves just oppositely to its electron counterpart in the *n*-type. For instance, comparisons between $J_{ph,d-\text{band}}^{(h)}$ and $J_{ph,s-\text{band}}^{(h)}$ in Cu with varying Cu film thicknesses and barrier heights are given in Fig. 6. As seen, $J_{ph,d-\text{band}}^{(h)}$ decreases as Φ_B is increased due to, again, the interband absorption edge at around –2.10 eV. The decrease in $J_{ph,d-\text{band}}^{(h)}$ with an increasing Φ_B at a fixed t_{Cu} is attributed to the diminishing permitted emission cone. However, $J_{ph,d-\text{band}}^{(h)}$ is a strong function of t_{Cu}, all dictated by much shorter MFPs that are determined by final energy states at which hot holes are generated.

Similar to $J_{ph,d-\text{band}}$ behaviors of the IPE in the *n*-type Schottky, $J_{ph,s-\text{band}}^{(h)}$ in the *p*-type is significantly affected by Φ_B owing to the shallow 4*s* states below E_F. Meanwhile, $J_{ph,s-\text{band}}^{(h)}$ is seen to decrease only mildly as t_{Cu} increases up to 100 nm. Referring to Fig. 4(b), since hot holes generated in shallow 4*s* states with their $E_{f,h}$'s within 0.5 eV away from E_F may typically have the MFPs larger than 100 nm, a trade-off between having a larger absorption depth (for generating more hot holes) and a smaller metal thickness (for minimizing scattering losses) is easier to achieve when compared to $J_{ph,d-\text{band}}$ from across the Cu-*n*-type Schottky.

C. Quantum yield analysis under AM1.5G solar irradiance spectrum

Figure 7 shows the QY comparisons for the Al- and Cu-*p* type Schottky barrier under direct transition approximations. Two metal thicknesses (t_{metal}) of 20 nm and 100 nm are considered as representative cases. Also shown in the figure are the results obtained in the framework of fully nondirect approximations for comparison purposes. In this approach, conservation of electron momentum is not considered and the corresponding EDJDOS is simply the product of the DOS at the initial and final energy levels times their corresponding occupancy probabilities[20]

$$\mathcal{D}_{\text{nondirect}}(E_{f,h}, h\nu) = \mathcal{N}(E_{f,h}) f(E_{f,h}) \mathcal{N}(E_{i,h}) \times \left[1 - f(E_{i,h})\right], \tag{22}$$

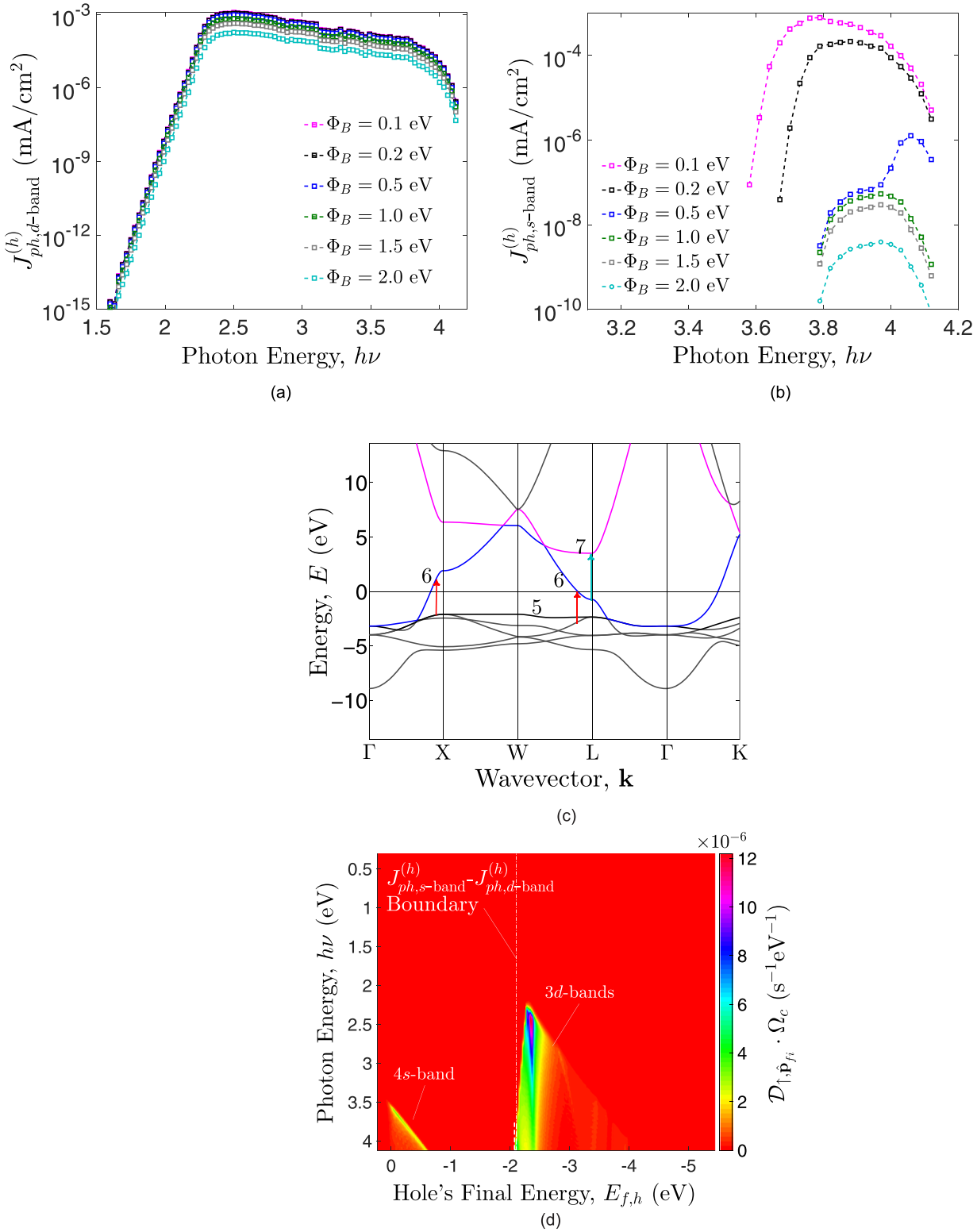

FIG. 5. Comparisons of the hole photocurrent density generated from (a) 3d bands and (b) the 4s band in Cu-p-type Schottky junction with varying photon energies at differing barrier heights. The Cu film is 20 nm in thickness. (c) Calculated band structure of Cu, showing allowed transitions mainly from band 6 to band 7 around the L point for $J^{(h)}_{ph,s-\text{band}}$. (d) Top view of $\mathcal{D}_{\uparrow,\tilde{\mathbf{p}}_{fi}} \cdot \Omega_c$ versus $E_{f,h}$ and $h\nu$ for Cu given in Fig. 2(b), where the boundary separating transitions from the 3d bands or from the 4s band is drawn and the energy distribution of hot holes is also clearly seen.

where $\mathcal{N}(E)$ denotes the DOS at energy level E and is given by[20]

$$\mathcal{N}(E) = \frac{2}{(2\pi)^3} \sum_j \int_{\text{FBZ}} \delta\left[E - E_{j,\mathbf{k}}\right] d^3\mathbf{k}. \tag{23}$$

Because of the parallel bands that are also parabolic-like in nature around E_F, η_{QY} in Al decreases monotonically with the increasing barrier height Φ_B, regardless of its film thickness. Note that such a decrease is also affected by the Φ_B-dependent momentum matching at the material interface,

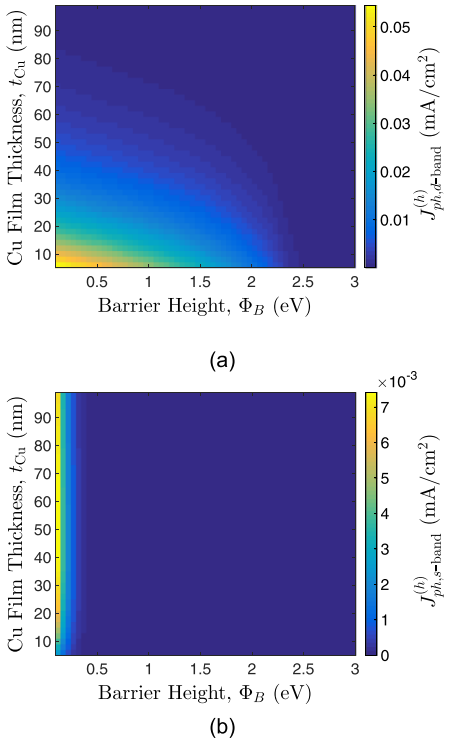

FIG. 6. Dependence of the hole photocurrent density on Cu film thickness t_{Cu} and barrier height Φ_B: contributed (a) from 3d bands and (b) from the 4s band.

in addition to the EDJDOS that generally decreases with $E_{f,h}$. Moreover, at $t_{metal} = 100$ nm [Fig. 7(b)], $\eta_{QY,Al} > 1\%$ for Φ_B up to 0.6 eV and stays above 0.1399% for $\Phi_B \leq 1.0$ eV, despite that the QY of Al exhibits a faster rate of decrease than that of Cu. Al losses its advantage over Cu when Φ_B goes beyond 2.05 eV. Similar Φ_B-dependence of the QY under direct and fully nondirect transitions is also clearly seen, suggesting the use of non-constant matrix elements in the calculations is perhaps not necessary in a free-electron-like band structure.

Also observed in Fig. 7(a) is the deflection point at $\Phi_B \approx 2.1$ eV for Cu. For $\Phi_B < 2.1$ eV, η_{QY} decreases gradually as Φ_B is increased. The decrease is mainly controlled by the momentum matching criterion upon emission since holes near the upper edge of the 3d-bands have sufficient excess energies to overcome the barrier. For $\Phi_B > 2.1$ eV, the precipitous drop of the EDJDOS and shorter MFPs of hot holes

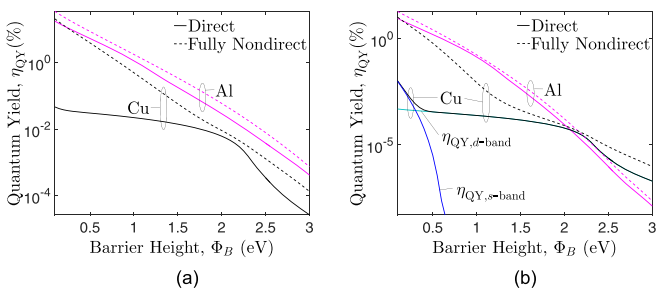

FIG. 7. Quantum yield (QY) investigations for Al and Cu with varying barrier heights at a metal film thickness t_{metal} of 20 nm (a) and 100 nm (b). Inelastic scattering and momentum matching upon emission are fully considered.

lead to the fast-decreasing η_{QY} in Cu. At $t_{Cu} = 100$ nm, the contribution from 4s band dominates the QY up to $\Phi_B \approx 0.3$ eV and is negligibly small for $\Phi_B > 0.45$ eV. It takes a thicker Cu film and a very small barrier height to reveal the contribution of 4s-state holes to the total hole photocurrent density and the QY.

D. Theoretical limits of power conversion efficiencies for Al and Cu

As the EDJDOS governs the vertical transition rate and the energy distribution of hot holes, whereas the barrier height and MFPs of holes together determine the reaching-emission probability P_{r-e}, the PCE of the IPE-based solar energy conversion may be optimized only for the barrier height Φ_B and the metal film thickness t_{metal} for a given metal. Neglecting bulk recombination losses, the net current density due to the IPE is given by[35]

$$J_{net} = J_{ph} - A^* T^2 e^{-\Phi_B/(k_B T)}\left[e^{eV/(k_B T)} - 1\right], \tag{24}$$

where A^* is the effective Richardson constant ($A^* = 120$ A K^{-2}cm^{-2} was assumed[18]), V the applied voltage, k_B the Boltzmann constant, and $T = 300$ K. The PCE is defined as the ratio of the maximum electrical power delivered to the load to the total power of the solar spectrum

$$\eta = \max(J_{net} \cdot V)\left[\int I_{\nu,AM1.5G}(\nu)d\nu\right]^{-1} \times 100\%. \tag{25}$$

Figure 8 depicts the maximum PCE as a function of barrier height and metal film thickness for Al and Cu. A threshold barrier energy for an appreciable PCE to occur is clearly

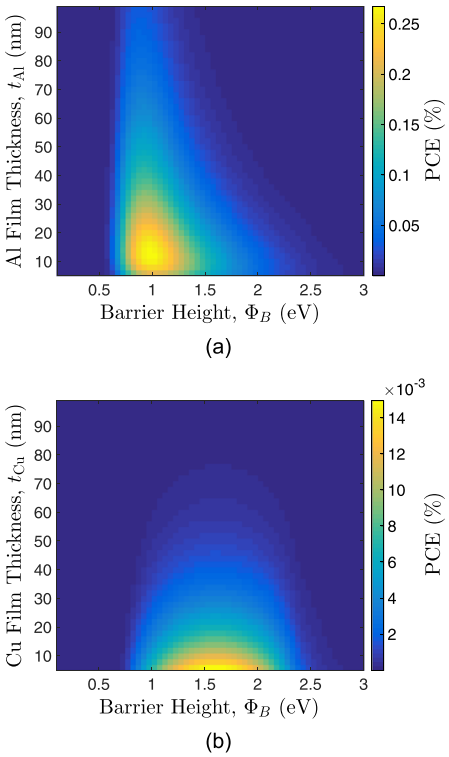

FIG. 8. Maximum power conversion efficiency (PCE) obtained from p-type Schottky junction with (a) Al and (b) Cu due to AM1.5G solar illumination.

seen for each metal, which is a direct result of requiring a sufficiently large Φ_B to effectively block the reverse thermionic current for an operational open-circuit voltage. For Al [Fig. 8(a)], the maximum PCE of 0.2673% is shown to occur at $\Phi_B \approx 0.95$ eV and $t_{Al} \approx 11.0$ nm (Table I). In fact, the PCE distribution across Φ_B and t_{Al} of interest is very similar to that in its *n*-type counterpart, where a constant momentum matrix element was assumed and **k**-resolved group velocities were not considered.[20] Also, since hot holes in Al have a more dispersive distribution of final energies, so do their MFPs. This allows wider ranges of Φ_B and t_{Al} within which the PCE stays above a fraction of 1%.

For Cu, its PCE across the Φ_B–t_{Cu} plane behaves just oppositely to that of Al. Since hot holes produced in the 3*d* bands constitute the majority of the photocurrent density, the PCE is less sensitive to the barrier height but is strongly dependent on the metal thickness (due to holes of higher excess energies). Still, the PCE is at least one order of magnitude smaller than that of Al. Similar differences have been revealed in the QY investigations and the major cause is the matrix-element-based EDJDOS that quantifies the influence of the band structure on direct transitions. The allowed direct transitions in Cu occur mainly near the L and X points; however, the highly dispersive 4*s* band with very limited density of states there ultimately restricts the number of transitions. Cu-based IPE in *p*-type Schottky surpasses its Al counterpart only when $\Phi_B \geq 2.2$ eV and $t_{metal} \geq 75$ nm.

IV. CONCLUSIONS

In summary, solar energy conversion via the IPE in a planar *p*-type Schottky junction has been investigated in the context of direct transitions with non-constant matrix elements H'_{fi}. Formulation of the (momentum) matrix element based on pseudo-wavefunction expansions has been developed to more accurately quantify the influence of band structure on direct transitions via the EDJDOS. For Al, the parabolic and "parallel-band" effect along the U-W-K path significantly enhances the EDJDOS across the entire energy axis. For Cu, the allowed transitions from 4*s* states near the L point are of narrowband character in both $E_{f,h}$ and $h\nu$ spectra ($E_{f,h} \approx [0.08, -0.67]$ eV, $h\nu \approx [3.49, 4.12]$ eV), while transitions from 3*d* states occur substantially near the upper edge of the 3*d* bands ($E_{f,h} \approx [-2.08, -2.44]$ eV) but are enabled by a relatively broad range of photon energies ($h\nu \approx [2.23, 4.12]$ eV). The average MFP of carriers in metals based on **k**-resolved group velocities exhibits asymmetric behaviors relative to the Fermi energy E_F. For Cu and Ag, a precipitous drop in the MFP at the interband absorption edge is observed and is smaller than 1 nm across the *d* bands.

The hole photocurrent density contributed by the 3*d* bands in Cu is of broadband character with a frequency bandwidth independent of the barrier height Φ_B but is strongly affected by the metal thickness. A smaller metal thickness enabling quasi-ballistic transport is thus in favor of the *d*-state hot holes. On the contrary, the hole photocurrent density from the 4*s* band of Cu is of narrowband character, exhibiting a high photon energy threshold and a strong dependence on Φ_B. Because of the shallow hole states in the 4*s* band that are typically within 0.6 eV below E_F, a trade-off between having a larger absorption depth (for generating more hot holes) and a shorter MFP (for minimizing scattering losses) exists for photon energy conversion using 4*s*-state holes.

Considering realistic band structure, **k**-resolved transition probabilities via H'_{fi}, carrier transport, momentum matching upon emission, and assuming zero reflectance at the air-metal interface, the PCE of IPE-based solar energy conversion (AM1.5G solar illumination) in Cu-*p*-type Schottky junction is shown to be less sensitive to Φ_B but is strongly dependent on the Cu film thickness t_{Cu}. Its theoretical limit is 0.0150% at $\Phi_B = 1.60$ eV and $t_{Cu} = 5.0$ nm. For Al, final energies of hot holes in Al are mainly within 1.41 eV below E_F but are also more dispersive across the energy spectrum. These characteristics enable a PCE up to 0.2673% at $\Phi_B = 0.95$ eV and $t_{Al} = 11.0$ nm and also allow a wider range of Φ_B and t_{Al} within which the PCE stays above a fraction of 1%. Because of the much higher transition rates across a fairly wide range of the energy spectrum and relatively longer MFPs without a sudden decrease, Al-*p*-type Schottky junction typically outperforms metals with relatively dispersionless *d*-bands in full-spectrum solar energy conversion.

TABLE I. Theoretical limits of power conversion efficiency (PCE) from internal photoemission in Al and Cu due to standard AM1.5G solar illumination. Non-constant momentum matrix elements [Eqs. (2) and (3)] are included in the direct transition formalism (Eq. 4). Inelastic scattering and momentum matching upon emission are fully considered.

	Direct transition			Fully nondirect approximation		
	Φ_B (eV)	t_{metal} (nm)	PCE (%)	Φ_B (eV)	t_{metal} (nm)	PCE (%)
Al	0.95	11.0	0.2673	1.00	11.0	0.4398
Cu	1.60	5.0	0.0150	0.90	9.0	0.1268

ACKNOWLEDGMENTS

This work was supported by the Ministry of Science and Technology, R.O.C. (Taiwan), under Grant No. MOST 103-2221-E-008-065-MY3.

[1]M. L. Brongersma, N. J. Halas, and P. Nordlander, Nat. Nanotechnol. **10**, 25 (2015).
[2]K. R. Catchpole and A. Polman, Opt. Express **16**, 21793 (2008).
[3]F. Wang and N. A. Melosh, Nano. Lett. **11**, 5426 (2011).
[4]Y. Takahashia and T. Tatsumab, Appl. Phys. Lett. **99**, 182110 (2011).
[5]A. K. Pradhan, T. Holloway, R. Mundle, H. Dondapati, and M. Bahoura, Appl. Phys. Lett. **100**, 061127 (2012).
[6]F. P. G. d. Arquer, A. Mihi, D. Kufer, and G. Konstantatos, ACS Nano **7**, 3581–3588 (2013).
[7]F. B. Atar, E. Battal, L. E. Aygun, B. Daglar, M. Bayindir, and A. K. Okyay, Opt. Express **21**, 7196 (2013).
[8]C. Clavero, Nat. Photonics **8**, 95 (2014).
[9]H. Chalabi, D. Schoen, and M. L. Brongersma, Nano Lett. **14**, 1374 (2014).
[10]F. Wang and N. A. Melosh, Nat. Commun. **4**, 1711 (2013).
[11]Y. Fang, Y. Jiao, K. Xiong, R. Ogier, Z.-J. Yang, S. Gao, A. B. Dahlin, and M. Käll, Nano Lett. **15**, 4059 (2015).
[12]M. Bernardi, J. Mustafa, J. B. Neaton, and S. G. Louie, Nat. Commun. **6**, 7044 (2015).

[13]C. Ng, J. J. Cadusch, S. Dligatch, A. Roberts, T. J. Davis, P. Mulvaney, and D. E. Gómez, ACS Nano **10**, 4704 (2016).
[14]Y. Nishijima, K. Ueno, Y. Yokota, K. Murakoshi, and H. Misawa, J. Phys. Chem. Lett. **1**, 2031 (2010).
[15]M. W. Knight, H. Sobhani, P. Nordlander, and N. J. Halas, Science **332**, 702 (2011).
[16]W. Li and J. Valentine, Nano Lett. **14**, 3510 (2014).
[17]T. P. White and K. R. Catchpole, Appl. Phys. Lett. **101**, 073905 (2012).
[18]A. J. Leenheer, P. Narang, N. S. Lewis, and H. A. Atwater, J. Appl. Phys. **115**, 134301 (2014).
[19]S. V. Boriskina, J. Zhou, W.-C. Hsu, B. Liao, and G. Chen, Proc. SPIE **9608**, 960816 (2015).
[20]Y.-J. Chang and K.-H. Shih, J. Appl. Phys. **119**, 183101 (2016).
[21]M. Fox, *Optical Properties of Solids* (Oxford University Press, Oxford, England, UK, 2007).
[22]A. D. Rakic, A. B. Djurisic, J. M. Elazar, and M. L. Majewski, Appl. Opt. **37**, 5271 (1998).
[23]R. Y. Koyama and N. V. Smith, Phys. Rev. B **2**, 3049 (1970).
[24]S.-L. Chuang, *Physics of Photonic Devices*, 2nd ed. (Wiley, 2009).
[25]A. M. Brown, R. Sundararaman, P. Narang, W. A. Goddard III, and H. A. Atwater, ACS Nano **10**, 957 (2016).
[26]A. O. E. Animalu and H. Heine, Philos. Mag. **12**, 1249 (1965).
[27]W. A. Harrison, *Pseudopotentials in the Theory of Metals* (W. A. Benjamin, 1966).
[28]C. Y. Fong, J. P. Walter, and M. L. Cohen, Phys. Rev. B **11**, 2759 (1975).
[29]C. Y. Fong and M. L. Cohen, Phys. Rev. Lett. **24**, 306 (1970).
[30]J. S. S. Commun, Solid State Commun. **12**, 303 (1973).
[31]J. Singh, *Physics of Semiconductors and their Heterostructures* (McGraw-Hill Education, 1993).
[32]M. Bauer, S. Pawlik, and M. Aeschlimann, Proc. SPIE **3272**, 201 (1998).
[33]J. J. Quinn, Phys. Rev. **126**, 1453 (1962).
[34]C. Kittel, *Introduction to Solid State Physics*, 8th ed. (Wiley, New York, 2004).
[35]S. J. Fonash, *Solar Cell Device Physics* (Elsevier, Burlington, MA, USA, 2010).